Engineering Structures 317 (2024) 118653

Contents lists available at ScienceDirect

Engineering Structures

journal homepage: www.elsevier.com/locate/engstruct

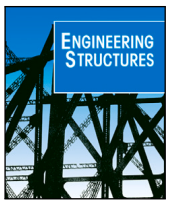

Dynamic analysis of the effects of vehicle movement over bridges observed with CCTV images

Alfredo Camara [a,*], Constantino Carlos Reyes-Aldasoro [b]

[a] Universidad Politécnica de Madrid, Department of Continuum Mechanics and Theory of Structures, Calle Profesor Aranguren 3, Madrid, 28040, Spain
[b] City, University of London, Department of Computer Science, Northampton Square, London, EC1V 0HB, UK

ARTICLE INFO

Dataset link: https://github.com/AlfredoCamaraC/MDyn, https://github.com/reyesaldasoro/Bridges

Keywords:
Image analysis
Modal dynamics
Traffic flow
Bridge vibrations
Comfort assessment

ABSTRACT

This work describes a combination of image analysis techniques used to identify vehicles travelling on a bridge with a vectorised modal dynamic analysis that can handle efficiently a large number of wheel loads on the deck at each analysis step-time. In the absence of weight-in-motion data, a randomisation of the traffic flow is proposed to define the weight of the vehicles as a function of their identified size. The methodology is applied to real CCTV recording on a conventional road bridge with a large width-to-span ratio in which the deck is modelled with shell elements. The latter is found to be important to capture the significant contribution of local slab modes to the vibrations along the sidewalks. The dynamic analysis of a large number of traffic records indicate that code-based load cases with long truck convoys lead to unrealistically large contributions of high-order modes and to vibrations that are categorised as uncomfortable, whilst the more realistic traffic flows obtained from image analysis satisfy the comfort criteria based on root-mean-square accelerations.

1. Introduction

Over the service life of a road bridge, real live actions consist of millions of fluctuating loads caused by the objects, mainly vehicles, that traverse over it. The vehicles can modify their speeds, change lanes or stop completely, depending on the actual traffic conditions, and it is essential to represent these accurately in fatigue life assessment, vehicle driving safety and users' comfort analyses.

In fatigue analysis, the traffic actions are traditionally over-simplified as scenarios of vehicles or convoys that are static or move at constant speeds [1–3], which hardly resemble the real vehicle actions. As a result, there is consensus on the need to improve the definition of the loading in fatigue life assessments [2,4]. On the other hand, most of the previous works on the driving safety and comfort analysis of road bridges consider a single moving vehicle at constant speeds (e.g. [5–17]) or a convoy of equally spaced vehicles moving in straight paths (e.g. [18–22]). Consequently, there is a growing interest on the definition of realistic traffic actions in bridges that account for the interactions between vehicles on the bridge. To this end, some research works microsimulate the movement of individual vehicles within traffic flows generated with cellular automata (CA) algorithms that discretise the space of the road into cells that can be either occupied by a vehicle or empty [23–28]. However, the discrete space–time nature of the CA vehicle models can lead to vehicle flows that are unrealistic for the dynamic analysis of the bridge.

Closed-circuit television (CCTV) recordings have been widely used in monitoring traffic [29–32], assessing the structural health of civil structures, especially analysing vibration [33–35], and assessing fire detection and incidents [36–38]. Recently, the use of CCTV video recordings have been proposed to obtain information about the actual traffic flows. Lee and Koh [39] used real-time video to identify the position of the vehicles and correlated it with sensors that measure the response of the bridge. Similarly, Dan et al. [40] proposed a methodology to identify moving loads to assess the health condition of bridges by merging the information of piezoelectric sensors and multiple cameras. The combination of images with sensors provide different signals for analysis, however, sensors are not always available, neither several cameras as suggested in [41]. Chen et al. [42] proposed an image processing technique to obtain from CCTV monitoring the position and velocity of vehicles crossing bridges. Unfortunately, this information was not applied to the structural analysis of a bridge. It can be attributed to the significant computational cost involved in the dynamic analysis of structures subject to long and stochastic traffic flows with large numbers of moving vehicles, which are needed to obtain representative results of the structural response [26–28]. A recent publication applied deep learning [43] to detect traffic and estimate the load distribution. The methodology required high-definition cameras that were strategically placed to look over the lanes on the bridge and thus simplifying the conditions of the vehicle segmentation.

* Corresponding author.
E-mail addresses: alfredo.camara@upm.es (A. Camara), reyes@city.ac.uk (C.C. Reyes-Aldasoro).

https://doi.org/10.1016/j.engstruct.2024.118653
Received 2 December 2023; Received in revised form 22 April 2024; Accepted 17 July 2024
Available online 29 July 2024

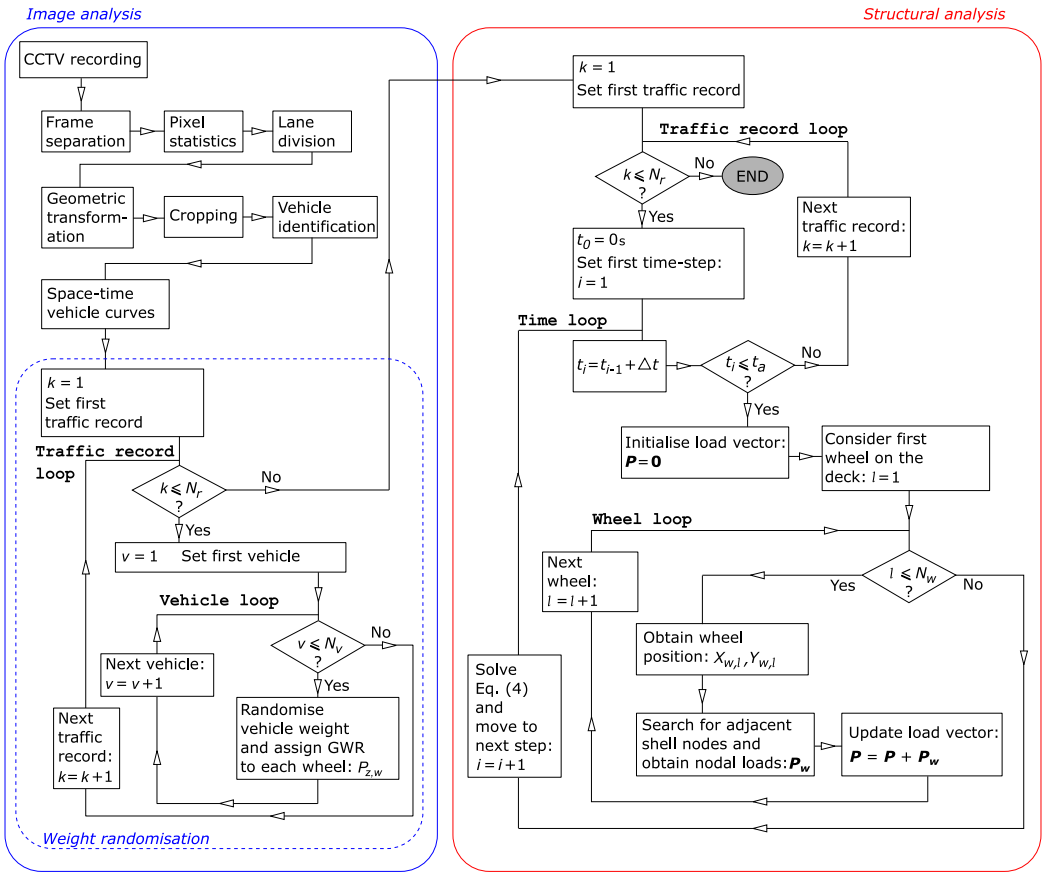

Fig. 1. Proposed analysis flowchart.

The present research contributes a new methodology that enables the CCTV monitoring system existing in most bridges to identify the position, speed and size of thousands of vehicles in real time, and feeds this information to a detailed structural analysis based on shell-like discretisations of the deck. In the absence of weigh-in-motion data, a randomisation of the identified vehicles' weight based on their size is proposed. In addition, efficient load-interpolation, vectorisation and sub-structuring techniques are also presented to reduce the computational cost of the modal dynamic analysis, and to enable the study of the response of bridges subject to long recorded traffic flows. This methodology is applied to a conventional road bridge, and it is observed that compared with the recorded traffic flows the traditional load cases based on equally spaced convoys of identical trucks lead to unrealistic vibrations along the sidewalks, both in terms of magnitude and frequency content.

2. Methodology and case study

The methodology proposed in this study combines image analysis with structural dynamics to obtain the response of bridges in time domain. Fig. 1 presents the analysis flowchart, which will be described as it is applied to the study of a road bridge monitored through a webcam. We select the case of the *Old Evripos Bridge* in Greece because it is constantly monitored (http://olne.gr/el/evripos-bridge/evripos-bridge-live-stream), with the camera and the website where the videos are accessible being operated by the Evia Island Ports Authority (OLNE S.A. https://olne.gr/). Fig. 2(a) shows the structure from a frame of a video taken by the webcam. It is noted that the real truss structure of the Old Evripos Bridge is not considered in the study. Instead, a more common ladder-deck composite bridge of the same span and width is proposed in order to increase the generality of the results obtained from the dynamic analysis.

2.1. Image analysis

First, the frames of the video recording of the bridge and its traffic are processed. These frames are used to detect individual objects (cars, vans, trucks) that move along the bridge in two directions. The pre-processing of the video consists of a pipeline of image processing techniques [44–46] with the following steps:

1. *Frame separation*: Frames of the video are selected as separate images. Due to memory constraints, for short videos ($t_a < 60$ s) all frames can be considered. For longer videos, four frames per second are suggested.
2. *Pixel statistics*: Mean, median and standard deviation along time are calculated for each pixel of the frame, and used to create a median image (Fig. 2(b)) and standard deviation image (Fig. 2(c)). The median image gives a representative frame where all the moving objects have been removed. This image is used later for the segmentation of the moving objects by subtracting the median from any given frame. The standard deviation image highlights the regions of the image where movement of objects occurred. This image is also useful to determine if the recording camera suffers movement (due to e.g. strong wind gusts), which would be revealed by variation of static elements in the field of view.
3. *Lane division*: The lanes of the bridge are the regions of interest for the study, and these are determined from the high intensity pixels of the standard deviation image (Fig. 3(a)). This region is further processed to find the centreline of the deck separating the traffic, and the orientation of the bridge (Fig. 3(b,c)) .
4. *Geometric transformation*: A geometric transformation [47] based on the previously determined orientation of the bridge is applied to the image to compensate for the perspective provided by

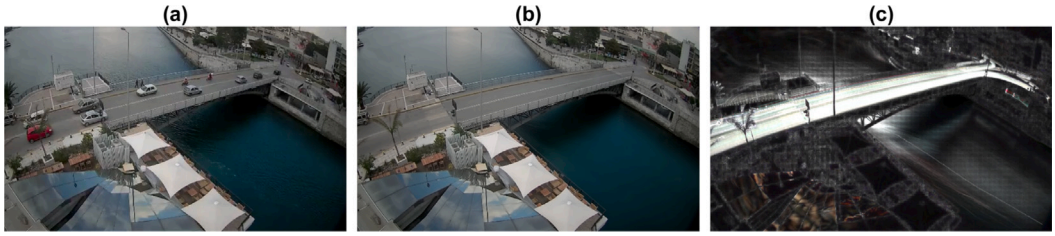

Fig. 2. Pre-processing of a 37-second video captured from the webcam of the old Evripos bridge in Greece. (a) One representative frame of the video showing a series of vehicles. (b) Extraction of the background by removal of all moving objects from the frames by calculating the median value of each pixel along the time dimension. (c) Accumulation of movement over time as the variation of each pixel against the background indicates the movement over the bridge. Notice also the movement of the water.

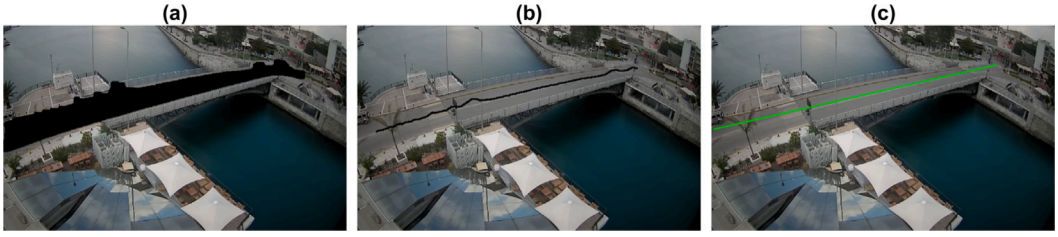

Fig. 3. Segmentation of the region of interest and extraction of orientation. (a) Segmentation of the lanes of the bridge. (b) Medial line from the segmentation. (c) Straight line adjusted to the Medial line. This line will be used to apply an affine transformation to all frames of the video.

the camera. In particular, this study applies a forward two-dimensional (2D) projective warp [48] with the following transformation matrix: $\begin{bmatrix} 1 & -0.031 & -0.0011 \\ 0.194 & 1 & 0.001 \\ 0 & 0 & 1 \end{bmatrix}$. This transformation compensates for the orientation and changing width of the view of the bridge provided by the camera, and it results in a *true* view with a horizontal deck of constant width. The median and standard deviation images are transformed in the same way and used in subsequent steps.

5. *Cropping*: The transformed image is cropped to focus on the region of interest over the bridge (Fig. 4).
6. *Vehicle identification*: The segmentation is performed by subtracting the average value of the red, green and blue channels (RGB) of the median image from every frame. Then, the intensity of the output is scaled to the range $[0-1]$ and thresholding using Otsu's method [49]. Morphological operators [50] (opening, labelling, closing) are employed to clean the objects, with a minimum size of object being applied to discard small artefacts. A particular challenge in the image processing of traffic occurs when tall vehicles like trucks appear as they could span both lanes of the bridge. These cases are identified by detecting large objects in each lane, when the horizontal span of each of these objects overlapped by more than 50% they are considered to be the same and only one was assigned. Pedestrians are excluded from the identification through the use of hand-drawn masks that concentrated on the two lanes (moving left or right).

Snippets of video from the webcam were saved to a local drive using the software QuickTime (*support.apple.com/quicktime*). Initial investigations were performed on a 37 s video recorded on the 25 July 2017, and a video of $t_a = 785$ s recorded on the 29 November 2021 was then used for the subsequent work in this paper. A representative image of the sequence is illustrated in Fig. 2(a). The output of the segmentation process provided one signal per object detected, i.e., a single vehicle would provide one signal at each frame it was detected. The fields of the vehicle signal consisted of: longitudinal position (along-drive, X) of the vehicle over the bridge in metres, lane of the bridge in which it is located to obtain the transverse position (Y, in metres), time in seconds and area of the vehicle in pixels. The space–time record of the whole traffic in the bridge is illustrated in Fig. 5 as (X_v, t) curves of the longitudinal position of the vth-vehicle along the deck (horizontal axis) versus the time (vertical axis going down). The slope of these curves gives the speed of each vehicle, which is limited to 30 km/h on the bridge.

The two lanes of the deck hold traffic in opposite directions. We consider positive movement the one that goes from left to right, with the origin of the system of coordinates located at the joint of the left abutment ($X = 0$), as shown in Fig. 6. Given that the position of the webcam and detail of the video was not sufficient to distinguish the transverse location of the vehicles accurately, it is assumed that they are centred on their lanes, with eccentricity $Y = \mp 1.75$ m with respect to the bridge centreline ($Y = 0$) in the Lanes 1 and 2 described in Fig. 6, respectively. All the code related to the image analysis was performed in the programming environment of Matlab® (The Mathworks™, Natick, USA) and is freely available through GitHub: https://github.com/reyesaldasoro/Bridges.

Unfortunately, the application of this image analysis process does not give information about the weight of each vehicle crossing the bridge, nor the Ground Wheel Reactions (GWR) that are needed in the structural analysis. The latter can only be determined if weight-in-motion (WIM) is available. In its absence, we propose a randomisation of the weight of the vehicles following the scheme presented in Fig. 1. The process creates from a single CCTV recording N_r random traffic records in which the space–time curves of each vehicle is identical, but their weight is obtained from a Gaussian distribution based on their approximate size, given by the average number of pixels associated with them.

Based on the identified traffic on the bridge, the flow is categorised into three different types of vehicles to simplify the randomisation of their weights, namely cars, vans, and light good vehicles (LGV). The distinction between them from the CCTV frames is based on the average number of pixels (Pix) of each identified object as it crosses the bridge. Table 1 gives the lower and upper limits of Pix for each vehicle category ($\text{Pix}^{\text{small}}$ and $\text{Pix}^{\text{large}}$, respectively). During the 785-s CCTV recording a total of 153 and 212 vehicles were identified in lanes 1 and 2, respectively, and according to the proposed categorisation these were distributed in 88 cars, 64 vans and 1 LGV in Lane 1, with 197 cars and 15 vans in Lane 2. It is noted that the moving objects with Pix < 500 refer to motorbikes and they are ignored in the analysis. For convenience, the wheel loads in the structural analysis are referred to the rear of each vehicle.

For simplicity, the dimensions of the vehicles and the distribution of the weight among their four wheels are only considered a function of

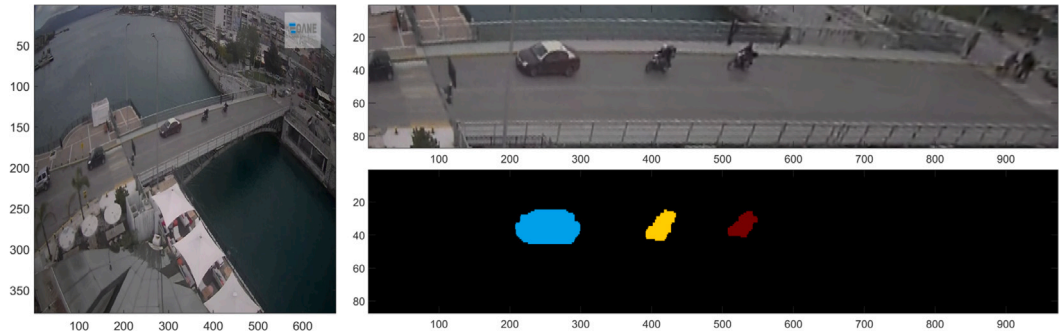

Fig. 4. Illustration of the transformation and segmentation. (left) One representative frame of the video, which shows one car and two motorcycles in the region of interest. (top) The same frame after warping and cropping. (bottom) Three segmented objects, each indicated by a different colour. (For interpretation of the references to colour in this figure legend, the reader is referred to the web version of this article.)

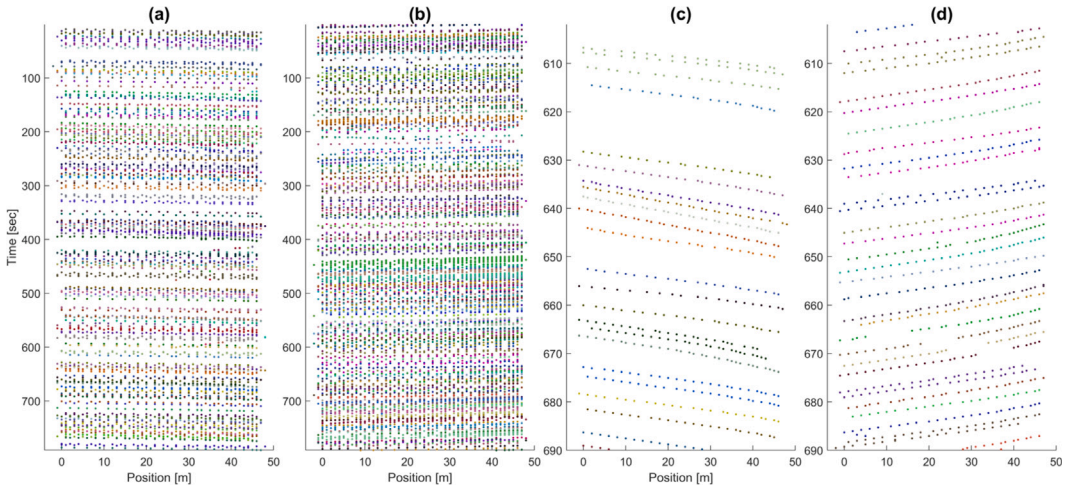

Fig. 5. Space–time vehicle curves obtained from the video, with each dot representing one object detected. (a) 4657 objects moving towards the right in Lane 1 grouped as 153 unique vehicles with single trajectory. (b) 7447 objects travelling towards the left in Lane 2 grouped as 212 unique vehicles with single trajectory. (c,d) Zoom in to a shorter time frame to illustrate the movement of the vehicles, each of which is denoted by a random colour for visualisation purposes. (For interpretation of the references to colour in this figure legend, the reader is referred to the web version of this article.)

Table 1
Geometry and dimensions of the vehicles considered in the structural analysis. Pix^{small} and Pix^{large} refer to the lower and upper limits of the pixel band for the corresponding vehicle. Note: the large HGV is based on the AASHTO HS20-44 truck [51] and it was not identified in the image analysis, instead, it is proposed for code-based calculations in Section 3. Dimensions in metres and weights in kN.

	Car	Van	LGV	HGV
Elevation	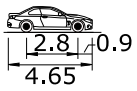	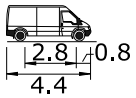	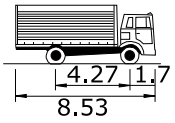	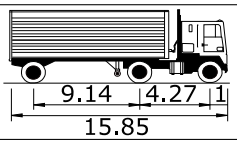
Plan: GWR	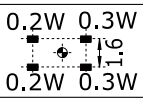	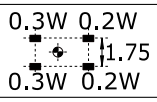	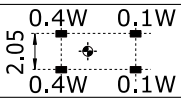	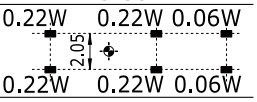
Pix^{small}	500	1500	2200	–
Pix^{large}	1500	2200	4000	–
Model small	Nissan Micra	Ford Transit Courier	Isuzu FRR 500	–
Model large	Audi A8	Ford Transit Custom	Iveco 180E25	–
a_{kerb}	0.008	0.023	0.027	–
b_{kerb}	7.7	−23.59	−23.90	–
$a_{\max,payload}$	0.002	0.030	0.039	–
$b_{\max,payload}$	2.7	−37.94	−62.78	–
$W_{\min,payload}$	0.5	0.5	0.5	–

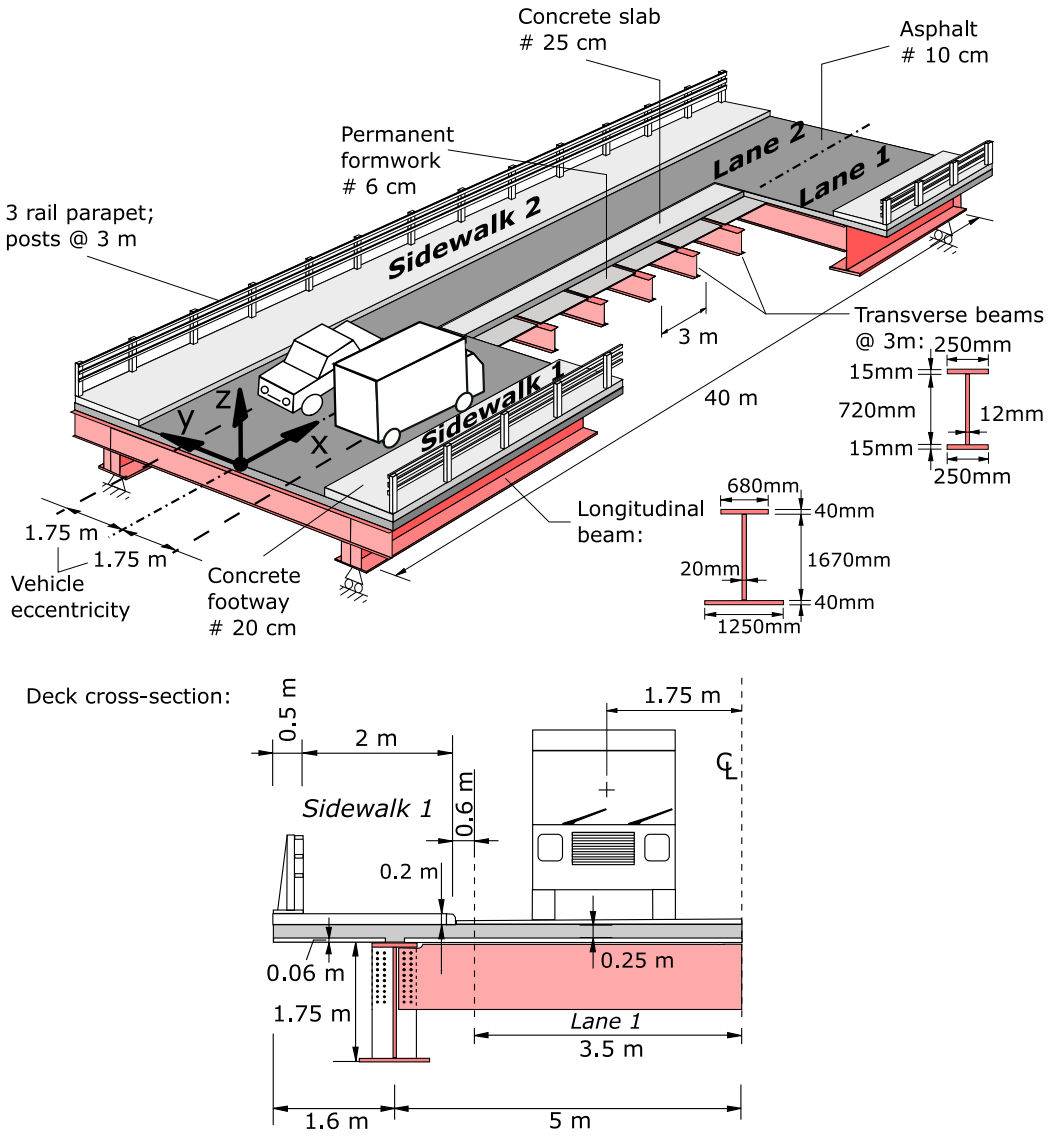

Fig. 6. Structural layout and dimensions of the proposed bridge. The symbol '#' refers to the thickness.

their category (car, van or LGV), and not their size (Pix). However, the latter affects the total weight of the vehicle W, which is the sum of its kerb (empty) weight, W_{kerb}, and its payload (cargo), $W_{payload}$, and it is different in each vehicle of the recorded traffic flow. The definition of the weight is based on data provided by manufacturers of vehicles taken as reference for the small and large bands of each vehicle category, included in Table 1.

The kerb weight is given as

$$W_{kerb} = a_{kerb}\text{Pix} + b_{kerb}, \tag{1}$$

in which a_{kerb} and b_{kerb} are the slope and the ordinate-intercept of the linear equation that we propose to define W_{kerb}, respectively, and they are given in Table 1 for the three different types of vehicles considered.

The randomisation of the traffic flow comes from the definition of the vehicle payload ($W_{payload}$), which is the most uncertain value given that we can only estimate its size from the CCTV recording, but not its contents. This weight is taken from a normal probability distribution $\mathcal{N}(\mu_{payload}, \sigma^2_{payload})$ centred in the mean value $\mu_{payload}$ with a standard deviation $\sigma_{payload}$, and it is limited between a minimum and a maximum payload as

$$W_{payload} = \max\left\{\min\left[W_{\max,payload}, \mathcal{N}\left(\mu_{payload}, \sigma^2_{payload}\right)\right], W_{\min,payload}\right\}, \tag{2}$$

where $W_{\min,payload}$ is the minimum payload in the vehicle, which is considered as 0.5 kN regardless of its size to consider an empty vehicle with only a relatively light-weight driver; $W_{\max,payload}$ is the maximum payload and it depends on the vehicle size as

$$W_{\max,payload} = a_{\max,payload}\text{Pix} + b_{\max,payload}, \tag{3}$$

with $a_{\max,payload}$ and $b_{\max,payload}$ obtained from the data provided by the manufacturers of vehicle models taken as representative in each vehicle category in Table 1. The mean value of the normal payload distribution is considered as the average between the minimum and the maximum values, and the standard deviation is assumed to be 20% the corresponding mean value in all the cases. The implications of this choice in the dynamic response of the bridge are discussed later in the paper.

For comparison purposes, two additional load cases with convoys of equally-spaced heavy goods vehicles (HGVs) are considered in the subsequent dynamic analysis: (1) HGVs crossing the bridge using only Lane 1, with the other lane completely empty, and (2) HGVs crossing the bridge using both lanes (Lane 1 in positive-X and Lane 2 in negative-X directions). In both cases the speed of the truck is kept constant at 30 km/h, and the distance between consecutive vehicles is calculated to give a time of 2 s between the rear of one truck and

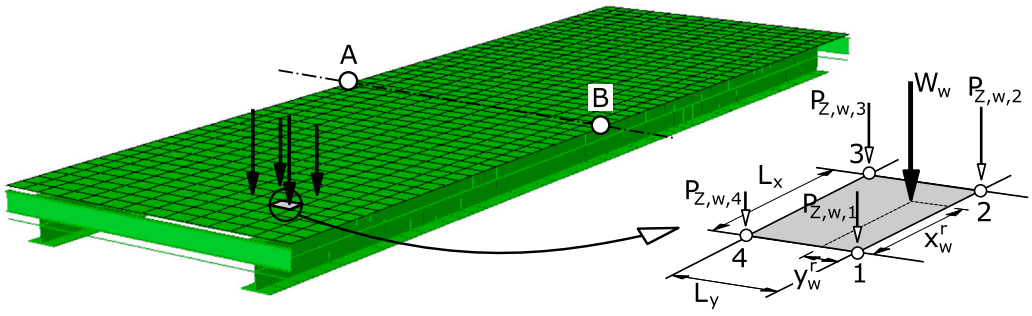

Fig. 7. FE model of the bridge and load interpolation of a single wheel.

the front of the following, resulting in a 25.3-m spacing between them. The convoys are composed of 259 trucks crossing the bridge in these additional load cases in order to have a complete analysis time of the same duration as with the image-processed flows ($t_a = 785$ s). The HGVs in these simplified load cases are based on the large AASHTO HS20-44 truck [51] that is described in Table 1, with a total weight of $W = 320$ kN.

2.2. Structural analysis

The proposed bridge is a 40-m span composite ladder-deck with a concrete slab supported by two longitudinal I-shaped steel girders that are connected by transverse beams at 3-m intervals, as shown in Fig. 6. The recorded traffic flow is applied to a finite element (FE) model of the bridge in which the slab is discretised with 728 full-integration 4-node shell elements of approximately 0.8×0.8 m, and a total of $N_d = 795$ nodes. The longitudinal and transverse steel beams are modelled with linear interpolation beam elements rigidly connected to the concrete slab. The distance between the centre of the supports and the girder end is 0.4 m. The two supports located under Sidewalk 2 restrain the lateral (Y) motion of the deck, whereas the other two release it, as it is illustrated in Fig. 6.

It is assumed that the response of the bridge under the traffic actions is linear and elastic. Therefore, the dynamic response of the structure can be obtained as the superposition of the time–history contribution of a reduced set of J vibration modes. The participation of the jth mode is given by the coordinate q_j and its time-derivatives ($\dot{q}_j$ and $\ddot{q}_j$) as

$$\ddot{q}_j(t) + 2\xi_j\omega_j\dot{q}_j(t) + \omega_j^2 q_j(t) = \frac{\boldsymbol{\phi}_j^{\mathrm{T}}\mathbf{P}(t)}{m_j}, \tag{4}$$

where $\boldsymbol{\phi}_j$, ω_j, ξ_j and m_j refer to the shape, circular frequency, damping ratio and mass of the jth mode, respectively. The accurate representation of the vibration modes requires great detail in the FE model to capture both the stiffness and the mass of the structure, including the structural mass and the non-structural one given by the asphalt (modelled as increased concrete density), parapets and sidewalks (represented with lumped masses at their corresponding positions). However, these details of the model are not explicitly included in the dynamic analysis of the traffic-induced vibrations. Instead, substructuring is proposed to speed up the dynamic analysis by considering only the modal displacements $\boldsymbol{\phi}_j$ corresponding to the slab of the deck, ignoring the degrees of freedom associated with the steel beams. This is possible because they are not directly loaded by the vehicles and therefore they do not contribute to the nodal forcing vector $\mathbf{P}(t)$. For convenience, in this work $\mathbf{P}$ is organised as follows

$$\mathbf{P}(t) = \{\underbrace{\mathbf{0}}_{\text{X-forces}}, \underbrace{\mathbf{0}}_{\text{Y-forces}}, \underbrace{P_{Z,1}(t), \ldots, P_{Z,N_d}(t)}_{\text{Z-forces}}\}^{\mathrm{T}}, \tag{5}$$

where $P_{Z,m}(t)$ is the vertical force at the mth node of the slab due to the vehicles on the deck at time t. Horizontal (braking) and lateral wheel forces are ignored in this study (hence $P_{X,m} = P_{Y,m} = 0$ at any node m), as well as the vehicle vibration and its interaction with the bridge. The latter can be included in the analysis methodology, but it requires the definition of the mechanical properties of the different types of vehicles crossing the bridge, and it would divert the attention from the goal of the study which focuses on the response of bridges (not the vehicles) under image-processed traffic flows.

The time-domain analysis requires a nested FOR-loop in which for each time-step of the analysis (outer layer) the contribution of each wheel on the deck (inner layer) to the nodal forcing vector in Eq. (5) is calculated, as shown in Fig. 1. The following is considered to speed up computation and make the analysis of long traffic flows feasible:

- *Discard from the analysis the vehicles that are not on the bridge*: In Eq. (4) it is only necessary to consider the vehicles with at least one wheel axle on the deck at a given time t_i of the analysis. Therefore, in this time-step the wheel-loop only needs to run over the N_w wheels of the vehicles on the bridge, which is smaller than the total number of vehicles registered in the CCTV image analysis (N_v). To this end, an *existence matrix* $\boldsymbol{\Lambda} = \{\Lambda_{i,v}\}$ is created for the observed traffic flow, prior to the dynamic analysis, with

$$\Lambda_{i,v} = \begin{cases} 1 & \text{if at least one axle of vehicle } v \text{ is on the bridge at time } t_i, \\ 0 & \text{otherwise.} \end{cases} \tag{6}$$

  Therefore, at each time t_i only the vehicles with $\Lambda_{i,v} = 1$ are considered in the dynamic analysis.
- *Accelerate the search of adjacent nodes*: One of the processes that is more computationally expensive is the search of the nodes adjacent to the position of each wheel on the deck. The use of traditional search functions in programming languages has a time-complexity $\mathcal{O}(N_d)$, and the calculation time increases linearly with the number of nodes in which it is searched. Instead, we propose a binary search that halves the search interval in each iteration, and it is significantly more efficient, with $\mathcal{O}(\log(N_d))$ [52]. The search is conducted independently in the longitudinal and transverse directions to find the shell element of the concrete slab that is directly loaded by each wheel w, which is facilitated by the structured mesh shown in Fig. 7. The wheel load is lumped to the 4 adjacent nodes as $P_{Z,w,kl} = \alpha_{kl} W_w$, with $kl = 1, 2, 3, 4$ referring to the local numbering of the shell element in Fig. 7 and the linear interpolation functions:

$$\alpha_1 = \left(1 - \frac{x_w^r}{L_x}\right)\left(1 - \frac{y_w^r}{L_y}\right), \tag{7a}$$

$$\alpha_2 = \left(\frac{x_w^r}{L_x}\right)\left(1 - \frac{y_w^r}{L_y}\right), \tag{7b}$$

$$\alpha_3 = \left(\frac{x_w^r}{L_x}\right)\left(\frac{y_w^r}{L_y}\right), \tag{7c}$$

$$\alpha_4 = \left(1 - \frac{x_w^r}{L_x}\right)\left(\frac{y_w^r}{L_y}\right), \tag{7d}$$

where x_w^r and y_w^r are the relative distances from the load to the local Node 1 of the loaded shell in the longitudinal and transverse directions, respectively; L_x and L_y are the corresponding element lengths (in this study $L_x \approx L_y \approx 0.8$ m).

- *Vectorisation of modal dynamics solver*: the traditional modal superposition requires repeating sequentially the calculation in Eq. (4) for all the vibration modes that are relevant to the response of the structure. This is avoided by computing the modal forcing $\hat{\mathbf{P}}$ with a matrix-multiplication of the mode shape matrix $\boldsymbol{\Phi}$ containing all the relevant eigenvectors ($\boldsymbol{\phi}_j$) times the lumped nodal loads given by all the wheels on the deck at the time t_i

$$\hat{\mathbf{P}} = \boldsymbol{\Phi}^{\mathrm{T}}\mathbf{P}, \tag{8}$$

in which it has been assumed that the modal shapes are mass-normalised. The array with the modal coordinates of all the relevant vibration modes ($\mathbf{q}$) can be obtained by introducing the modal forcing $\hat{\mathbf{P}}$ in the right-hand side of Eq. (4) and solving it simultaneously with the non-iterative and vectorised Newmark-β method described in [53]. Finally, the response of the structure at time t_i and its time-derivatives are obtained directly as:

$$r(t_i) = \boldsymbol{\Phi}\mathbf{q}(t_i);\ \dot{r}(t_i) = \boldsymbol{\Phi}\dot{\mathbf{q}}(t_i);\ \ddot{r}(t_i) = \boldsymbol{\Phi}\ddot{\mathbf{q}}(t_i). \tag{9}$$

The FE model of the structure was conducted in the software Abaqus [54] to obtain the vibration modes with all the necessary detail (including the steel, concrete and non-structural elements). The most relevant ones are included in Fig. 8. The fundamental mode is a global vertical flexure of the deck ($f_1 = 2.01$ Hz) and the second one describes its global torsion ($f_2 = 2.88$ Hz). Due to the large width-to-span ratio of the bridge higher-order vibration modes involve transverse flexure of the slab. Mode 3 ($f_3 = 3.75$ Hz) shows a localised transverse flexure close to the abutments, and modes 4 to 13 involve the transverse flexure of the slab between the two longitudinal girders, but their modal displacements along the sidewalks are generally smaller. However, there is a range of modes between 18 and 50 Hz with relevant excitation of the sidewalks. These are referred to as *slab modes* and it will be demonstrated later that they are important for the accelerations that could be sensed by pedestrians. Therefore, the first $J = 60$ vibration modes are considered in the dynamic analysis, and the time-step is set as $\Delta t = 0.002$ s to capture accurately all the relevant modes (below 50 Hz). It is noted that the analysis time-step is smaller than that with which the CCTV recording in the bridge is processed (0.25 s), therefore linear interpolation was applied to find the position of the vehicles in the intervals between consecutive video frames.

For each random traffic record k the dynamic response of the bridge is obtained by implementing the proposed methodology in the Python library MDyn [53], which is freely available at: https://github.com/AlfredoCamaraC/MDyn. The damping ratio is considered $\xi = 0.5\%$ for all the vibration modes, following [7,8,55]. The total time of the analysis in each record is $t_a = 785$ s, which coincides with the duration of the CCTV image processing. A total of $N_k = 100$ different records of the traffic loading are considered.

3. Results and discussion

Fig. 9 shows a representative time interval of the dynamic vertical displacement of the bridge at midspan (sidewalk edge points A and B in Fig. 7) when the structure is subject to the randomised image-processed traffic flows, with cars, vans and LGVs crossing the structure in both traffic lanes. The results in this figure represent the mean of the 100 randomised traffic flow records obtained from the image analysis. In addition, the displacements obtained with the simplified load cases based on convoys of AASHTO trucks are included in the figure. The cadence of the passing trucks in the convoy load cases is clear from the results, with an excitation interval of approximately 3 s (0.33 Hz) given by the constant spacing between trucks and their speed. This contrasts with the more random response of the bridge under the recorded traffic, which also gives significantly lower displacements due to the smaller loads compared with those of large HGV trucks. As expected, the peak displacements are similar in both sidewalks in the load cases for which both lanes are occupied, but for the case with trucks in lane 1 exclusively the general torsion of the bridge is activated and the displacements at Point B (i.e. in the sidewalk next to the loaded lane) are larger.

The record-to-record variability of the randomised image-processed signals in the vertical displacements at the same two points at midspan is presented in Fig. 10 for a narrower time window. It is observed that a variance of $\sigma^2 = 0.04\mu^2$ in the vehicles' mean cargo (μ) introduces a variability in the peak dynamic displacements at midspan of up to 22%. More specifically, the peak displacement at midspan at Point B range from 1.53 to 1.62 mm in the 100 records considered, and it goes from 1.46 to 1.88 mm at point A. The peak displacement of 1.88 mm occurs for record #40, which will be considered further in the discussion as it gives the largest response of the bridge.

The dynamic effects of the moving vehicles on the bridge are obtained by comparing the dynamic displacements obtained from Eq. (4) and their purely static counterparts. The latter are obtained from the same traffic flows by cancelling the damping and inertia terms in Eq. (4):

$$q_j^{st}(t_i) = \frac{\boldsymbol{\phi}_j^{\mathrm{T}}\mathbf{P}(t_i)}{\omega_j^2}, \tag{10}$$

where q_j^{st} is the static coordinate of mode j, and it is assumed that the vibration mode shapes are mass-normalised. After a sensitivity analysis to define the number of modes considered in the static analysis, the total static response (r^{st}) is obtained as the superposition of the contribution of the first $J = 60$ modes:

$$r^{st}(t_i) = \boldsymbol{\Phi}\mathbf{q}^{\mathbf{st}}(t_i). \tag{11}$$

Fig. 11 compares the vertical static and dynamic bridge displacements at point B under the recorded traffic flow with largest response (record #40), and also under the two load cases with convoys of AASHTO trucks. It is apparent that the inertia forces increase the displacements of the bridge, for which the dynamic response presents a characteristic frequency of approximately 3 Hz that is related to the second vibration mode of the bridge shown in Fig. 8, as it will be explored in more detail later.

The dynamic impact factor at the mth node of the deck slab is defined as

$$\mathrm{IF}_m = \frac{\max_{t_i}\left[|r_m(t_i)|\right]}{\max_{t_i}\left[|r_m^{st}(t_i)|\right]}, \tag{12}$$

in which r_m and r_m^{st} are the dynamic and static displacements at node m, respectively. The IF is included in Fig. 12 for all the nodes along the edges of both sidewalks, and it is compared with the value recommended by AASHTO to account for traffic-induced dynamic effects in the static analysis of road bridges (IF = 1.33). The typical values of the IF obtained in this bridge are below this limit and oscillate around 1.15. However, close to the supports of the deck the vertical static displacements are very small and make the definition of the IF in Eq. (12) more unreliable. For the same reason, the IF of the response along sidewalk 2 is higher in the load case with a convoy of trucks concentrated in lane 1, because the torsion generated reduces the vertical displacement in the opposite sidewalk (Fig. 12(a)). Nevertheless, it is interesting to note that despite the larger weight of the vehicles crossing the bridge in the two load cases with HGV convoys, the dynamic amplification of the displacements in most of the length of Sidewalk 1 is similar to

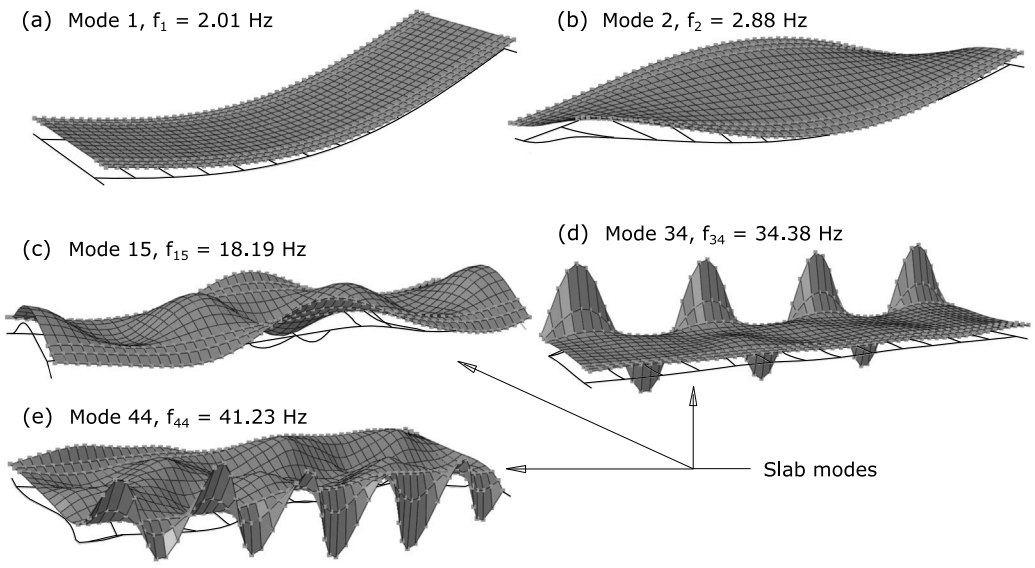

Fig. 8. Relevant vibration modes of the bridge and their natural frequencies f.

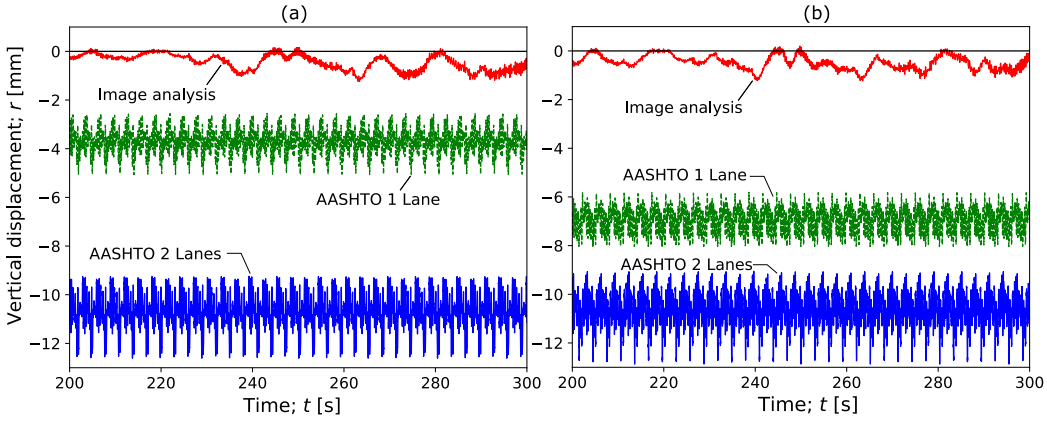

Fig. 9. Time–history of the vertical displacement at midspan: (a) point A, (b) point B.

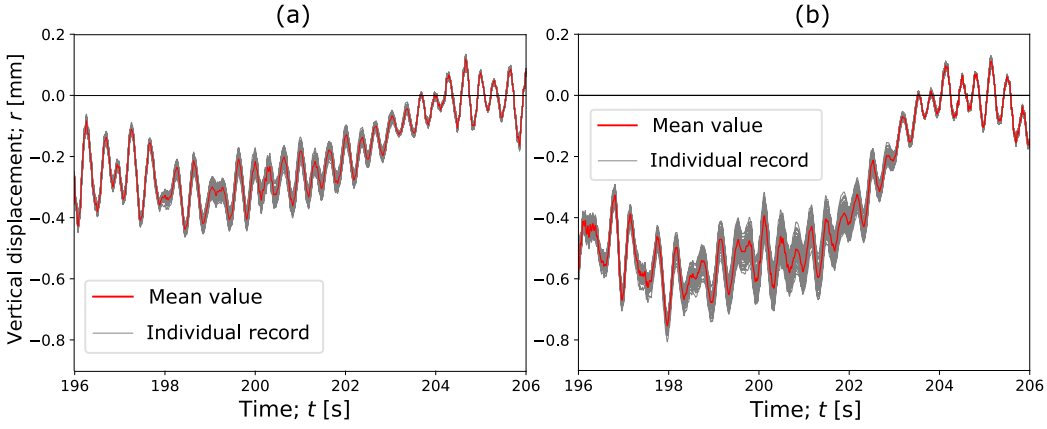

Fig. 10. Detail of the time–history of the vertical displacement at midspan due to the recorded traffic: (a) point A, (b) point B.

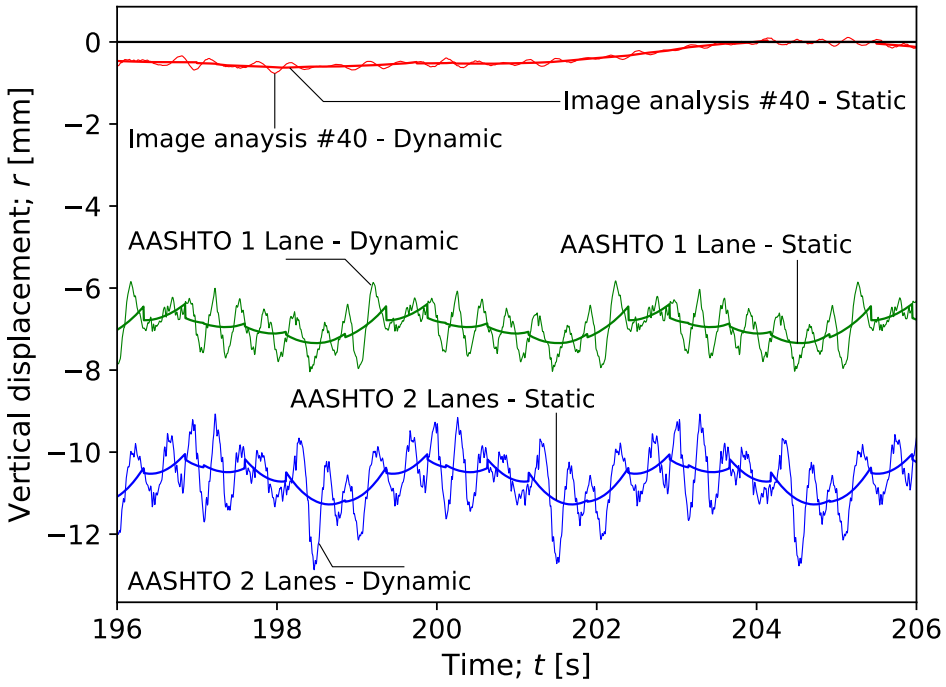

Fig. 11. Comparison between the dynamic and the static responses at point B of the deck, for different load cases.

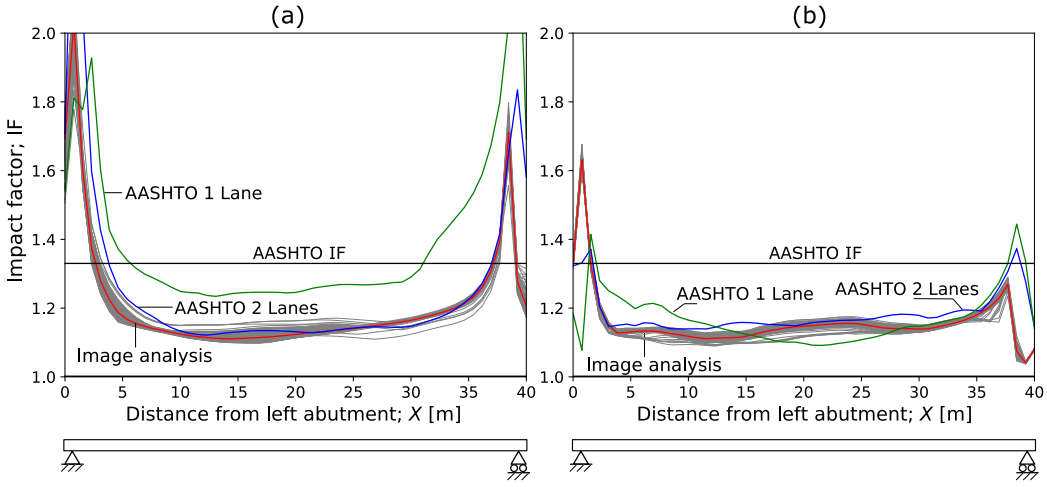

Fig. 12. Dynamic impact factor along the sidewalk edges of the bridge: (a) sidewalk 2, (b) sidewalk 1.

that observed with the image-processed traffic. In addition, the record-to-record variability of the IF obtained with the latter is relatively small (below 4% at midspan), which suggests that considering the mean value of the vehicle weight distribution gives a reasonable value of the dynamic traffic-induced effects in this type of bridges.

3.1. Comfort analysis

The assessment of the pedestrians' comfort on the sidewalks of the bridge depends on the frequency content of its vibrations (e.g. [16,19,56]). The evolution of the contribution of different frequencies to the vertical displacements and accelerations at point A (sidewalk 2) as the image-processed traffic record #40 excites the bridge is presented in the spectrograms of Figs. 13(a) and (b), respectively. The results in Fig. 13(a) indicate that the displacement response at midspan is dominated by the low-order vibration modes 1 and 2 (see Fig. 8), whereas the slab modes above 18 Hz with local flange deformation at the sidewalk areas have lower contribution, particularly in the intervals with less recorded traffic on the bridge at $t \sim 50$ s, 220 s and 360 s, as shown in Fig. 5. The displacement signal also captures the static effect of the vehicle entrance in the bridge, with an average frequency of 0.46 Hz (given by the access of 365 vehicles to the deck in 785 s). However, the pedestrians' comfort depends on the accelerations, and Fig. 13(b) indicates that these are more influenced by high-order slab modes, especially modes 15 and 34, which is in agreement with previous works on bridges with large width-to-span ratios [14,19].

The effect of the gaps in the actual vehicle flow recorded by CCTV make the frequency content time-dependent. This contrasts with the uniform bands of modal contribution when the bridge is subject to the code-based convoys of heavy trucks shown in Fig. 14. These load cases exaggerate the participation of high-order modes above 20 Hz, particularly modes 34 and 44 included in Fig. 8. Therefore, it seems important to consider more realistic vehicle flows in the dynamic analysis.

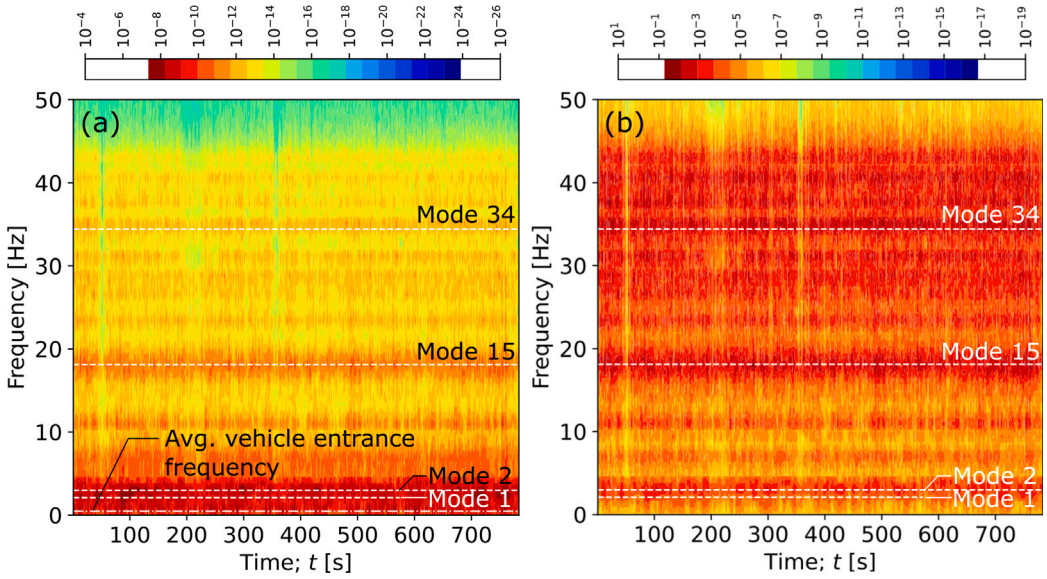

Fig. 13. Spectrogram of the vertical response of the bridge at midspan of sidewalk 2 (point A) due to the recorded traffic (record #40): (a) displacements, (b) accelerations.

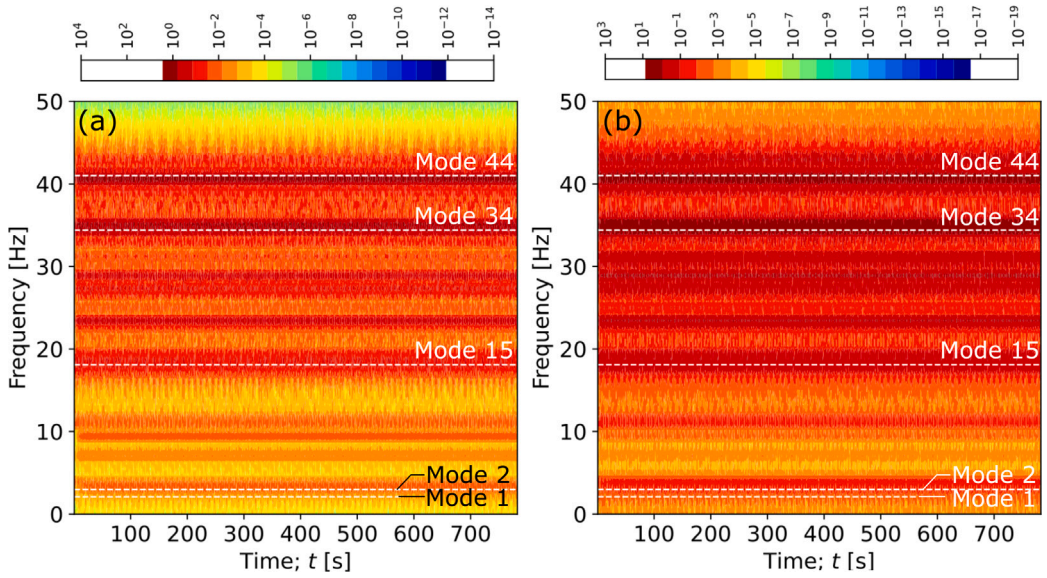

Fig. 14. Spectrogram of the vertical response of the bridge at midspan of sidewalk 2 (point A) due to the AASHTO truck loading: (a) trucks in one lane, (b) trucks in two lanes.

We use Irwin's criterion [57] to assess the comfort of pedestrians standing on the sidewalks of the bridge. To this end, the root-mean-square (RMS) of the acceleration signal $\ddot{r}(t)$ is calculated at different one-third octave bands as:

$$\ddot{r}_{\mathrm{RMS}}(f_c) = \sqrt{\int_{f_l}^{f_u} S_{\ddot{r}\ddot{r}}\,\mathrm{d}f}, \tag{13}$$

in which $S_{\ddot{r}\ddot{r}}$ is the Power Spectral Density (PSD) of the acceleration signal $\ddot{r}(t)$; f_l and f_u are the lower and the upper frequencies of each octave band, respectively. The RMS acceleration ($\ddot{r}_{\mathrm{RMS}}$) at each octave band is allocated to their central frequency f_c, for which the lower and upper frequencies are $f_l = 2^{-1/6} f_c$ and $f_u = 2^{1/6} f_c$, respectively. Finally, the calculated $\ddot{r}_{\mathrm{RMS}}$ is compared with the frequency-dependent comfort limit suggested by Irwin for frequent conditions [57] in Fig. 15, for different load cases. It is observed that the vibrations at the midspan section induced by the convoys of heavy trucks are categorised as uncomfortable, in both sidewalks. This is due to the effect of the first global torsional mode of the bridge (mode 2) and the high-order slab modes, and it is particularly large in sidewalk 2 due to the laterally-restrained support conditions at this side of the bridge. However, the comfort limits are not exceeded under any of the randomised image-processed traffic flows, for which mode 1 gives the RMS acceleration that is closest to the discomfort threshold. The recorded traffic cases lead to a significantly lower participation of the high-order slab modes in the pedestrians' sense of vibrations, compared with that obtained under the long convoys of equally-spaced trucks. In addition, the latter load cases present unrealistic peaks of $\ddot{r}_{\mathrm{RMS}}$ for frequencies significantly lower than that of the first bridge mode: $f_{l1} = 0.33$ Hz and $f_{l2} = 2f_{l1} = 0.66$ Hz, which are given by the artificial excitation frequency of the convoy of trucks.

Finally, the comfort assessment is extended to the entire length of both sidewalks by means of a discomfort risk ratio η

$$\eta_m = \max_f \left[\frac{\ddot{r}_{\mathrm{RMS},m}(f)}{\ddot{r}_{lim}(f)} \right], \tag{14}$$

in which the subindex m refers to the node of the sidewalk where it is calculated, and $\ddot{r}_{lim}(f)$ is the maximum admissible RMS acceleration

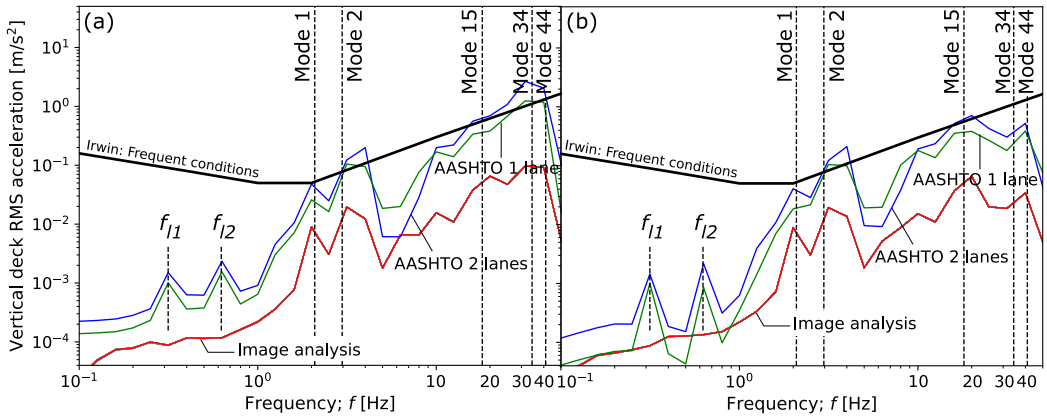

Fig. 15. Vertical RMS accelerations at midspan for different load cases: (a) point A in sidewalk 2, (b) point B in sidewalk 1. Note that the image analysis presents the results of 100 random records in grey colour, but they are almost superimposed to their mean value, depicted in red colour. (For interpretation of the references to colour in this figure legend, the reader is referred to the web version of this article.)

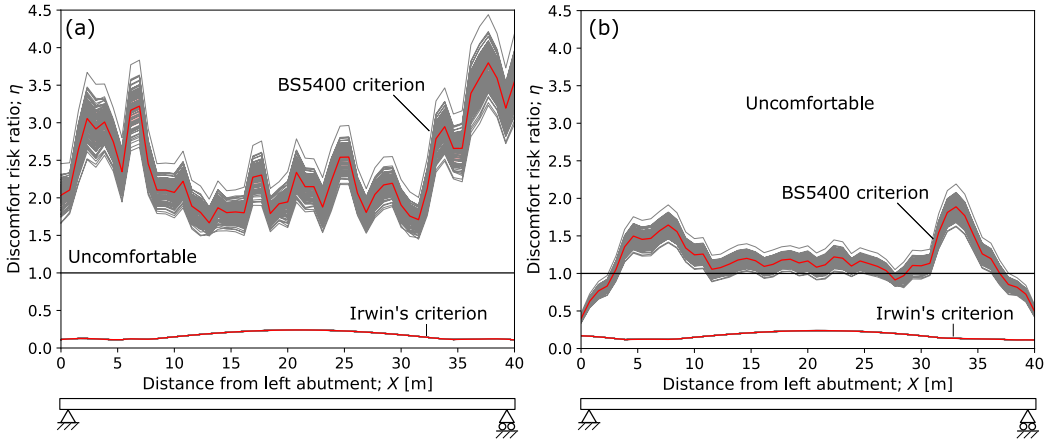

Fig. 16. Discomfort risk ratio along the sidewalk edges of the bridge under all the image analysis records: (a) sidewalk 2, (b) sidewalk 1. The thin grey lines refer to the results for each individual traffic record, the thicker red line is their arithmetic mean, and the coloured band around it represents one standard deviation to each side of the mean value. (For interpretation of the references to colour in this figure legend, the reader is referred to the web version of this article.)

proposed by Irwin in frequent conditions (see Fig. 15). In addition, vibrations are assessed based on the peak accelerations along the sidewalks considering the BS5400 comfort criteria [58]:

$$\eta_m = \frac{\max_t[|\ddot{r}_m(t)|]}{\ddot{r}_{lim}}, \tag{15}$$

with $\ddot{r}_{lim} = 0.5\sqrt{f_1} = 0.71$ m/s^2 being the maximum admissible peak acceleration given in [58], and $f_1 = 2.01$ Hz is the fundamental vertical frequency of the bridge.

The discomfort risk ratios obtained for both comfort criteria along the sidewalks are included in Fig. 16, considering the accelerations induced by the 100 different image-processed traffic flows. The record-to-record variability within the randomised traffic flows is significant (up to 33%) in terms of the peak accelerations, which exceed the BS5400 comfort limit in most of the bridge sidewalk areas, particularly in the sidewalk 2 due to the lateral constrain of the supports at that side of the bridge. However, considering a more accurate comfort criteria based on the RMS accelerations reduces significantly the influence of the vehicle payload weight variability, with a record-to-record variation below 2%, and it makes it possible to consider a single traffic record with mean vehicle weight distributions. In addition, the RMS-based comfort criterion is satisfied in the entire bridge under the recorded traffic flows.

4. Conclusions

This work presents a methodology to combine CCTV image processing and modal structural dynamics to analyse the traffic-induced vibrations in bridges, without the need for monitoring or weight-in-motion data. The image analysis techniques are used to identify the motion of vehicles on a real bridge in Greece, and a randomisation process is proposed to generate records with different plausible weights based on the size of the observed vehicles. The work follows by introducing a method to define the modal forcing in shell-like finite element discretisations of the deck, which is applied to the model of a conventional ladder-deck composite bridge. The dynamic analysis of the structure under a significant number of traffic flows and convoy-based load cases led to the following observations:

- A standard deviation of the vehicle payload fixed as 20% of their mean value results in record-to-record differences of up to 22% and 33% in the peak displacements and accelerations at midspan, respectively. However, the variability is reduced below 4% and 2% in the dynamic impact factor and the RMS accelerations at the same section, making it possible to run the dynamic analysis for a single traffic record with assumed mean values of the vehicles' payload, in the absence of weight-in-motion data or more detailed image analysis of the moving vehicles with high-resolution CCTV recording.

- The unrealistic load cases composed only of heavy trucks crossing the bridge equally spaced and with constant speed exaggerate the contribution of high-order vibration modes with local flexure of the slab at the flanges where the sidewalks are located, leading to vibrations that are categorised as uncomfortable. However, the comfort criterion based on RMS accelerations is satisfied in the entire length of the sidewalks with all the recorded traffic flows.
- It is observed that the transverse flexure of the slab and the boundary conditions of the supports in this direction are important for the vibrations in the sidewalks. Therefore, to capture these effects it is recommended to discretise the upper slab with shell elements, which can be separated for efficiency from the rest of the structural and non-structural members of the finite element model in the modal analysis, as proposed in the paper.

This work aimed at establishing a framework where new image processing and artificial intelligence techniques can be applied in further studies to analyse in real time the response of bridges from CCTV recording, therefore assisting in the assessment of discomfort and fatigue risks in structures.

Nevertheless, the present work has several limitations related to the image processing of the videos. The first point to notice is that the video recordings were relatively short, that is, in the order of minutes and not hours. Relatively short videos were acquired because the objective was to demonstrate the methodology and to assess real traffic at certain times, but not the continuous monitoring of the bridge. If the goal is the continuous monitoring of the structure, the change in conditions from day to night or to a rainy day would require a dynamic calculation of the background to compensate with the changes in illumination. Second, camera shaking was not experienced in any of the videos acquired, however, this could happen under special conditions of strong wind or earthquakes. Third, the angle of the camera provided a good unobstructed view of one of the lanes of the bridge, but the other lane experience occlusions when large vehicles (lorries or buses) traversed the bridge. Fourth, as the video was not of high resolution, it was not possible to obtain details such as licence plates that could be then used to precisely identify the kerb weight of the vehicles (with the adequate data protection considerations) as it is done in some toll bridges or roads in certain countries. Finally, the resolution and angle of the images could not be used to evaluate the weight in motion by estimating the passengers or load of each vehicle, and for this reason we propose a randomisation of the vehicle loads that is proven valid for comfort assessments. It is also worth noting that the proposed methodology can be used to assess whether material or fatigue damage is initiated, particularly if it is combined with sensors of the actual response of the bridge at certain points, but it does not allow for a detailed study of the evolution of damage as it is based on modal superposition.

CRediT authorship contribution statement

Alfredo Camara: Writing – review & editing, Writing – original draft, Visualization, Validation, Software, Methodology, Investigation, Formal analysis, Conceptualization. **Constantino Carlos Reyes-Aldasoro:** Writing – original draft, Software, Methodology, Formal analysis, Data curation.

Declaration of competing interest

The authors declare that they have no known competing financial interests or personal relationships that could have appeared to influence the work reported in this paper.

Data availability

The analysis source files and relevant data used in this paper are freely available through the following GitHub repositories:

https://github.com/AlfredoCamaraC/MDyn: MDyn Python code related to the structural dynamic analysis.
https://github.com/reyesaldasoro/Bridges: Matlab code related to the image analysis.

Other data is available from the authors upon reasonable request.

Acknowledgements

The authors would like to express their gratitude to Dr. Panagiotis Mergos for his valuable comments and the initial guidance to find CCTV bridge monitoring data.

References

[1] Guo T, Frangopol D, Chen Y. Fatigue reliability assessment of steel bridge details integrating weigh-in-motion data and probabilistic finite element analysis. Comput Struct 2012;112–113:245–57.
[2] Lu N, Noori M, Liu Y. Fatigue reliability assessment of welded steel bridge decks under stochastic truck loads via machine learning. J Bridge Eng 2017;22(1):04016105.
[3] Zhu J, Zhang W. Probabilistic fatigue damage assessment of coastal slender bridges under coupled dynamic loads. Eng Struct 2018;166:274–85.
[4] Ye X, Su Y, Han J. A state-of-the-art review on fatigue life assessment of steel bridges. Math Probl Eng 2014;956473, 1–13.
[5] Xu Y, Guo W. Dynamic analysis of coupled road vehicle and cable-stayed bridge systems under turbulent wind. Eng Struct 2003;25:473–86.
[6] Xu Y, Guo W. Effects of bridge motion and crosswind on ride comfort of road vehicles. J Wind Eng Ind Aerodyn 2004;92:641–62.
[7] Cai C, Chen S. Framework of vehicle-bridge-wind dynamic analysis. J Wind Eng Ind Aerodyn 2004;92:579–607.
[8] Chen S, Cai C. Accident assessment of vehicles on long-span bridges in windy environments. J Wind Eng Ind Aerodyn 2004;92:991–1024.
[9] Guo W, Xu Y. Safety analysis of moving road vehicles on a long bridge under crosswind. J Eng Mech 2006;132(4):438–46.
[10] Oliva J, Goicolea J, Antolin P, Astiz M. Relevance of a complete road surface description in vehicle-bridge interaction dynamics. Eng Struct 2013;56:466–76.
[11] Camara A, Nguyen K, Ruiz-Teran A, Stafford P. Serviceability limit state of vibrations in under-deck cable-stayed bridges accounting for vehicle-structure interaction. Eng Struct 2014;61:61–72.
[12] Wang B, Xu Y, Zhu L, Li Y. Crosswind effect studies on road vehicle passing by bridge tower using computational fluid dynamics. Eng Appl Comput Fluid Mech 2014;8(3):330–44.
[13] Kavrakov I, Camara A, Morgenthal G. Influence of aerodynamic model assumptions on the wind-vehicle-bridge interaction. In: IABSE symposium. 2016, p. 1165–72.
[14] Camara A, Vazquez V, Ruiz-Teran A, Paje S. Influence of the pavement surface on the vibrations induced by heavy traffic in road bridges. Can J Civil Eng 2017;12(44):1099–111.
[15] Yang J, Ouang H, Stancioiu D. Numerical studies of vibration of four-span continuous plate with rails excited by moving car with experimental validation. Int J Struct Stab Dyn 2017;17(10):1750119.
[16] Nguyen K, Camara A, Rio O, Sparowitz L. Dynamic effects of turbulent crosswind on the serviceability state of vibrations of a slender arch bridge including wind-vehicle-bridge interaction. J Bridge Eng 2017;22(11):6017005.
[17] Yu H, Wang B, Li Y, Zhang Y, Zhang W. Road vehicle-bridge interaction considering varied vehicle speed based on convenient combination of simulink and ansys. Shock Vib 2018;1389628.
[18] Huang D. Vehicle-induced vibration of steel deck arch bridges and analytical methodology. J Bridge Eng 2012;17(2):241–8.
[19] Camara A, Ruiz-Teran A. Multi-mode traffic-induced vibrations in composite ladder-deck bridges under heavy moving vehicles. J Sound Vib 2015;355:264–83.
[20] Han Y, Cai C, Zhang J, Chen S, He X. Effects of aerodynamic parameters on the dynamic responses of road vehicles and bridges under crosswinds. J Wind Eng Ind Aerodyn 2014;134:78–95.
[21] Wang W, Han W, Kong W. Wind-vehicle-bridge coupled vibration analysis based on random traffic flow simulation. J Traffic Transp Eng 2014;4(1):293–308.
[22] Camara A, Kavrakov I, Nguyen K, Morgenthal G. Complete framework of wind-vehicle-bridge interaction with random road surfaces. J Sound Vib 2019;458:197–217.
[23] Chen S, Wu J. Dynamic performance simulation of long-span bridge under combined loads of stochastic traffic and wind. J Bridge Eng 2010;15(3):219–30.
[24] Wu J, Chen S. Probabilistic dynamic behavior of a long-span bridge under extreme events. Eng Struct 2011;33:1657–65.
[25] Zhou Y, Chen S. Fully coupled driving safety analysis of moving traffic on long-span bridges subjected to crosswind. J Wind Eng Ind Aerodyn 2015;143:1–18.

[26] Yin X, Wang L, Kong B, Song G, Liu Y. Probability analysis of the vibration of bridges with rough surface under stochastic traffic. Int J Struct Stab Dyn 2018;18(9):1850108.
[27] Zhu J, Xiong Z, Xiang H, Huang X, Li Y. Ride comfort evaluation of stochastic traffic flow crossing long-span suspension bridge experiencing vortex-induced vibration. J Wind Eng Ind Aerodyn 2021;219:104794.
[28] Hou G, Chen S, Chen F. Framework of simulation-based vehicle safety performance assessment of highway system under hazardous driving conditions. Transp Res C 2019;105:23–36.
[29] St-Aubin P, Saunier N, Miranda-Moreno L. Large-scale automated proactive road safety analysis using video data. Transp Res C 2015;58:363–79.
[30] Semertzidis T, Dimitropoulos K, Koutsia A, Grammalidis N. Video sensor network for real-time traffic monitoring and surveillance. IET Intell Transp Syst 2010;4(2):103.
[31] Sonnleitner E, Barth O, Palmanshofer A, Kurz M. Traffic measurement and congestion detection based on real-time highway video data. Appl Sci 2020;10(18):6270.
[32] Barthélemy J, Verstaevel N, Forehead H, Perez P. Edge-computing video analytics for real-time traffic monitoring in a smart city. Sensors 2019;19(9):2048.
[33] Chen JG, Davis A, Wadhwa N, Durand F, Freeman WT, Büyüköztürk O. Video camera–based vibration measurement for civil infrastructure applications. J Infrastruct Syst 2017;23(3).
[34] Zona A. Vision-based vibration monitoring of structures and infrastructures: An overview of recent applications. Infrastructures 2020;6(1):4.
[35] Medhi M, Dandautiya A, Raheja JL. Real-time video surveillance based structural health monitoring of civil structures using artificial neural network. J Nondestruct Eval 2019;38(3).
[36] Flores Quiroz N, Walls R, Cicione A, Smith M. Fire incident analysis of a large-scale informal settlement fire based on video imagery. Int J Disaster Risk Reduct 2021;55:102107.
[37] Ahn Y, Choi H, Kim BS. Development of early fire detection model for buildings using computer vision-based cctv. J Build Eng 2023;65:105647.
[38] Chiu C-W, Lu T, Chao H-T, Shu C-M. Performance assessment of video-based fire detection system in tunnel environment. Tunnell Underground Space Technol 2014;40:16–21.
[39] Lee D, Koh B. An image-based deep learning network technique for structural health monitoring, smart structures and systems. Int J 2021;28(6):799–810.
[40] Dan D, Ge L, Yan X. Identification of moving loads based on the information fusion of weigh-in-motion system and multiple camera machine vision. Measurement 2019;144:155–66.
[41] Bai Y, Demir A, Yilmaz A, Sezen H. Assessment and monitoring of bridges using various camera placements and structural analysis. J Civil Struct Health Monit 2023;14(2):321–37.
[42] Chen Z, Feng Y, Zhang Y, Liu J, Zhu C, Chen A. An accurate and convenient method of vehicle spatiotemporal distribution recognition based on computer vision. Smart Struct Syst Int J 2022;22(7):6437.
[43] Ge L, Dan D, Li H. An accurate and robust monitoring method of full-bridge traffic load distribution based on yolo-v3 machine vision. Struct Control Health Monit 2020;27(12).
[44] Gonzalez RC, Woods RE. Digital image processing. 4th ed.. Pearson; 2018.
[45] Reyes-Aldasoro CC. Biomedical image analysis recipes in MATLAB: for life scientists and engineers. 1st ed.. Wiley-Blackwell; 2015.
[46] Sonka M, Hlavac V, Boyle R. Image processing, analysis and machine vision. Springer; 1993.
[47] Berger M. Geometry. Springer Verlag; 2004.
[48] Wolberg G. Digital image warping. Wiley-IEEE Computer Society Press; 1990.
[49] Otsu N. A threshold selection method from gray-level histograms. IEEE Trans Syst Man Cybern 1979;9(1):62–6.
[50] Serra J. Introduction to mathematical morphology. Comput Vis Graph Image Process 1986;35(3):283–305.
[51] AASHTO. LRFD bridge design specifications. 2nd ed.. 1998.
[52] Tarek A. Binary search algorithm. In: American conference on applied mathematics. 2008, p. 104–9.
[53] Camara A. A fast mode superposition algorithm and its application to the analysis of bridges under moving loads. Adv Eng Softw 2021;151:102934.
[54] ABAQUS version 2022. 2022.
[55] EN1991-2, eurocode 1: Actions on structures - part 2: Traffic loads on bridges, EN 1991-2:2003. 2003.
[56] Camara A, Nguyen K, Ruiz-Teran A, Stafford P. Serviceability limit state of vibrations in under-deck cable-stayed bridges accounting for vehicle-structure interaction. Eng Struct 2014;61:61–72.
[57] Irwin A. Human response to dynamic motion of structures. Struct Eng 1978;56A(9):237–44.
[58] BS 5400-2. Steel, concrete and composite bridges - part-2: Specification for loads. 2006.